Astronomy
&
Astrophysics

Stellar laboratories

III. New Ba V, Ba VI, and Ba VII oscillator strengths and the barium abundance in the hot white dwarfs G191−B2B and RE 0503−289[*],[**],[***]

T. Rauch[1], K. Werner[1], P. Quinet[2,3], and J. W. Kruk[4]

[1] Institute for Astronomy and Astrophysics, Kepler Center for Astro and Particle Physics, Eberhard Karls University, Sand 1,
72076 Tübingen, Germany
e-mail: rauch@astro.uni-tuebingen.de
[2] Astrophysique et Spectroscopie, Université de Mons – UMONS, 7000 Mons, Belgium
[3] IPNAS, Université de Liège, Sart Tilman, 4000 Liège, Belgium
[4] NASA Goddard Space Flight Center, Greenbelt, MD 20771, USA

ABSTRACT

Context. For the spectral analysis of high-resolution and high-signal-to-noise (S/N) spectra of hot stars, state-of-the-art non-local thermodynamic equilibrium (NLTE) model atmospheres are mandatory. These are strongly dependent on the reliability of the atomic data that is used for their calculation.
Aims. Reliable Ba V-VII oscillator strengths are used to identify Ba lines in the spectra of the DA-type white dwarf G191−B2B and the DO-type white dwarf RE 0503−289 and to determine their photospheric Ba abundances.
Methods. We newly calculated Ba V-VII oscillator strengths to consider their radiative and collisional bound-bound transitions in detail in our NLTE stellar-atmosphere models for the analysis of Ba lines exhibited in high-resolution and high-S/N UV observations of G191−B2B and RE 0503−289.
Results. For the first time, we identified highly ionized Ba in the spectra of hot white dwarfs. We detected Ba VI and Ba VII lines in the Far Ultraviolet Spectroscopic Explorer (FUSE) spectrum of RE 0503−289. The Ba VI/Ba VII ionization equilibrium is well reproduced with the previously determined effective temperature of 70 000 K and surface gravity of $\log g = 7.5$. The Ba abundance is $3.5 \pm 0.5 \times 10^{-4}$ (mass fraction, about 23 000 times the solar value). In the FUSE spectrum of G191−B2B, we identified the strongest Ba VII line (at 993.41 Å) only, and determined a Ba abundance of $4.0 \pm 0.5 \times 10^{-6}$ (about 265 times solar).
Conclusions. Reliable measurements and calculations of atomic data are a pre-requisite for stellar-atmosphere modeling. Observed Ba VI-VII line profiles in two white dwarfs' (G191−B2B and RE 0503−289) far-ultraviolet spectra were well reproduced with our newly calculated oscillator strengths. This allowed to determine the photospheric Ba abundance of these two stars precisely.

Key words. atomic data – line: identification – stars: abundances – stars: individual: G191−B2B – stars: individual: RE 0503−289 – virtual observatory tools

1. Introduction

In recent analyses of the hydrogen-rich DA-type white dwarf (WD) G191−B2B (effective temperature $T_{\mathrm{eff}} = 60\,000$, surface gravity $\log(g/\mathrm{cm/s^2}) = 7.6$, Rauch et al. 2012, 2013, 2014) and the hydrogen-deficient DO-type WD RE 0503−289 ($T_{\mathrm{eff}} = 70\,000$, $\log g = 7.5$, Werner et al. 2012; Rauch et al. 2014), numerous lines of the trans-iron elements Zn, Ga, Ge, As, Se, Kr, Mo, Sn, Te, I, and Xe were identified. This substantially reduced the number of unidentified lines in the spectra of these two WDs. For precise abundances determinations, reliable transition probabilities are mandatory – these are necessary not only

for the identified lines themselves but for the complete model atom that is considered in the model-atmosphere and spectral-energy-distribution (SED) calculations. Thus, abundance determinations were so far restricted to Zn (Rauch et al. 2014), Ge (Rauch et al. 2012), Kr, Xe (Werner et al. 2012), and Sn (Rauch et al. 2013).

A close inspection of the still unidentified lines in the far-ultraviolet (FUV) spectrum of RE 0503−289 showed absorption features at the locations of the strongest Ba VI and Ba VII lines as given by NIST[1]. Therefore, we calculated Ba V-VII transition probabilities (Sect. 2) and employed our NLTE[2] model-atmosphere code (Sect. 4) to perform test calculations (Sect. 5) to find the strongest Ba lines in the model. Then, we used these strategic lines to determine the Ba abundances of G191−B2B and RE 0503−289 and searched for other, weak Ba lines (Sect. 6). We summarize our results and conclude in Sect. 7.

---

[*] Based on observations with the NASA/ESA *Hubble* Space Telescope, obtained at the Space Telescope Science Institute, which is operated by the Association of Universities for Research in Astronomy, Inc., under NASA contract NAS5-26666.

[**] Based on observations made with the NASA-CNES-CSA Far Ultraviolet Spectroscopic Explorer.

[***] Tables 1–3 are only available at the CDS via anonymous ftp to cdsarc.u-strasbg.fr (130.79.128.5) or via http://cdsarc.u-strasbg.fr/viz-bin/qcat?J/A+A/566/A10

[1] National Institute of Standards and Technology, http://www.nist.gov/pml/data/asd.cfm

[2] Non-local thermodynamic equilibrium.

2. Transition probabilities in Ba V, Ba VI, and Ba VII

Very few studies have been focused on the determination of electric dipole transition rates in Ba V, Ba VI, and Ba VII so far. To our knowledge, the only available data were recently published by Sharma et al. (2014) and Sharma et al. (2013) for Ba V and Ba VII, respectively. More precisely, these authors reported oscillator strengths and transition probabilities computed using rather limited configuration interaction models based on the Hartree-Fock approach due to Cowan (1981) combined with a semi-empirical least-squares fit of radial energy parameters. In order to get a uniform set of oscillator strengths for all the transitions of Ba ions observed in the present work, we decided to perform new calculations including a larger amount of electron correlation and hence improving the previous investigations of Sharma et al. (2013, 2014). The method adopted here was the relativistic Hartree-Fock (HFR) approach with core-polarization corrections (see e.g., Quinet et al. 1999, 2002).

For Ba V, configuration interaction was considered among the configurations $5s^25p^4$, $5s^25p^34f$, $5s^25p^35f$, $5s^25p^36f$, $5s^25p^37f$, $5s^25p^36p$, $5s^25p^37p$, $5s^25p^24f^2$, $5s^25p^25d^2$, $5s^25p^26s^2$, $5s^25p^26p^2$, $5s^25p^25d6s$, $5s^25p^24f6p$, $5s5p^45d6s$, $5s5p^46d$, $5s5p^46s$, and $5p^6$ for the even parity, and $5s5p^5$, $5s^25p^35d$, $5s^25p^36d$, $5s^25p^37d$, $5s^25p^36s$, $5s^25p^37s$, $5s^25p^24f5d$, $5s^25p^24f6d$, $5s^25p^24f6s$, $5s^25p^25d6p$, $5s^25p^26s6p$, $5s5p^44f$, $5s5p^45f$, $5s5p^46f$, and $5s5p^46p$ for the odd parity. The core-polarization parameters were the dipole polarizability of a Ba IX ionic core as reported by Fraga et al. (1976), i.e., α_d = 0.54 a.u., and the cut-off radius corresponding to the HFR mean value $\langle r \rangle$ of the outermost core orbital (4d), i.e., r_c = 0.79 a.u. Using experimental energy levels reported by Sharma et al. (2014), the radial integrals (average energy, Slater, spin-orbit and effective interaction parameters) of $5s^25p^4$, $5s^25p^36p$, $5s5p^5$, $5s^25p^35d$, and $5s^25p^36s$ configurations were optimized by a well-established least-squares fitting procedure in which the mean deviations with experimental data were found to be equal to 185 cm^{-1} for the even parity and 217 cm^{-1} for the odd parity.

For Ba VI, the configurations included in the HFR model were $5s^25p^3$, $5s^25p^24f$, $5s^25p^25f$, $5s^25p^26f$, $5s^25p^27f$, $5s^25p^26p$, $5s^25p^27p$, $5s^25p4f^2$, $5s^25p5d^2$, $5s^25p6s^2$, $5s^25p6p^2$, $5s^25p5d6s$, $5s^25p4f6p$, $5s5p^35d$, $5s5p^36d$, $5s5p^36s$, and $5p^5$ for the odd parity, and $5s5p^4$, $5s^25p^25d$, $5s^25p^26d$, $5s^25p^27d$, $5s^25p^26s$, $5s^25p^27s$, $5s^25p4f5d$, $5s^25p4f6d$, $5s^25p4f6s$, $5s^25p5d6p$, $5s^25p6s6p$, $5s5p^34f$, $5s5p^35f$, $5s5p^36f$, and $5s5p^36p$ for the even parity. In this ion, the semi-empirical process was performed to optimize the radial integrals corresponding to $5s^25p^3$, $5s5p^4$, $5s^25p^25d$, and $5s^25p^26s$ configurations using the experimental levels reported by Tauheed & Joshi (1994). The mean deviations between calculated and experimental energy levels were 5 cm^{-1} and 128 cm^{-1} for odd and even parities, respectively. Core-polarization effects were estimated using the same α_d and r_c values as those considered in Ba V.

Finally, a similar model was used in the case of Ba VII for which the $5s^25p^2$, $5s^25p4f$, $5s^25p5f$, $5s^25p6f$, $5s^25p7f$, $5s^25p6p$, $5s^25p7p$, $5s^24f^2$, $5s^25d^2$, $5s^26s^2$, $5s^26p^2$, $5s^25d6s$, $5s^24f6p$, $5s5p^25d$, $5s5p^26d$, $5s5p^26s$, and $5p^4$ even-parity configurations and the $5s5p^3$, $5s^25p5d$, $5s^25p6d$, $5s^25p7d$, $5s^25p6s$, $5s^25p7s$, $5s^24f5d$, $5s^24f6d$, $5s^24f6s$, $5s^25d6p$, $5s^26s6p$, $5s5p^24f$, $5s5p^25f$, $5s5p^26f$, and $5s5p^26p$ odd-parity configurations were explicitly included in the HFR model. Here also, we used the same core-polarization parameters as those considered for Ba V. The semi-empirical optimization process was carried out to adjust the radial parameters in $5s^25p^2$, $5p^4$, $5s^25p4f$, $5s^25p6p$, $5s5p^25d$, $5s5p^3$, $5s^25p5d$, and $5s^25p^26s$ with the experimental energy

Table 4. Statistics of our Ba model atom.

Ion	NLTE levels	LTE levels	Lines
Ba IV	1	6	0
V	123	0	981
VI	47	0	162
VII	121	0	452
VIII	1	0	0

levels classified by Sharma et al. (2013) below 350 000 cm^{-1} and 320 000 cm^{-1} for even and odd parities, respectively. In fact, it was found that many levels above those limits overlap unknown levels and are strongly mixed with states belonging to higher configurations such as $5s^24f^2$ (even parity), $5s5p^24f$, $5s^24f5d$, and $5s^25p6d$ (odd parity). It was then extremely difficult to establish an unambiguous correspondence between the calculated values and the experimentally determined level energies. The use of radial parameters published by Sharma et al. (2013) was unfortunately not of great help for making the identifications more reliable, the set of interacting configurations being not the same as the one considered in our work. For the levels considered in our fitting process, the mean deviations between calculated and experimental values were found to be equal to 140 cm^{-1} (even parity) and 196 cm^{-1} (odd parity).

Figure 1 shows Grotrian diagrams of Ba V-VII including all levels and transitions from Tables 1–3.

3. Observations

In this analysis, we use the FUSE[3] spectrum of RE 0503−289 and the FUSE and HST/STIS[4] spectra of G191−B2B that are described in detail by Werner et al. (2012) and Rauch et al. (2013, 2014), respectively.

The FUSE spectrum covers the wavelength range 910 Å $< \lambda <$ 1188 Å. Its resolving power is $R = \lambda/\Delta\lambda \approx 20\,000$. The HST/STIS spectrum of G191−B2B is co-added from 105 observations with the highest resolution (grating E140H, $R \approx 118\,000$, 1145 Å $< \lambda <$ 1750 Å) available via MAST.

4. Model atmospheres and atomic data

Our model atmospheres (plane-parallel, chemically homogeneous, in radiative and hydrostatic equilibrium) were calculated with the Tübingen NLTE model-atmosphere package (TMAP[5], Werner et al. 2003; Rauch & Deetjen 2003).

The model atoms (including Ba, Table 4 displays its statistics) that are considered in our calculations are provided by the Tübingen Model-Atom Database (TMAD[6], Rauch & Deetjen 2003), that was constructed in the framework of the German Astrophysical Virtual Observatory (GAVO[7]). The SEDs that were calculated for this analysis are available via the registered Theoretical Stellar Spectra Access (TheoSSA[8]) VO service.

---

[3] Far Ultraviolet Spectroscopic Explorer.

[4] *Hubble* Space Telescope/Space Telescope Imaging Spectrograph, for our high-resolution spectrum of G191−B2B, see http://www.stsci.edu/hst/observatory/crds/calspec.html

[5] http://astro.uni-tuebingen.de/~TMAP

[6] http://astro.uni-tuebingen.de/~TMAD

[7] http://www.g-vo.org
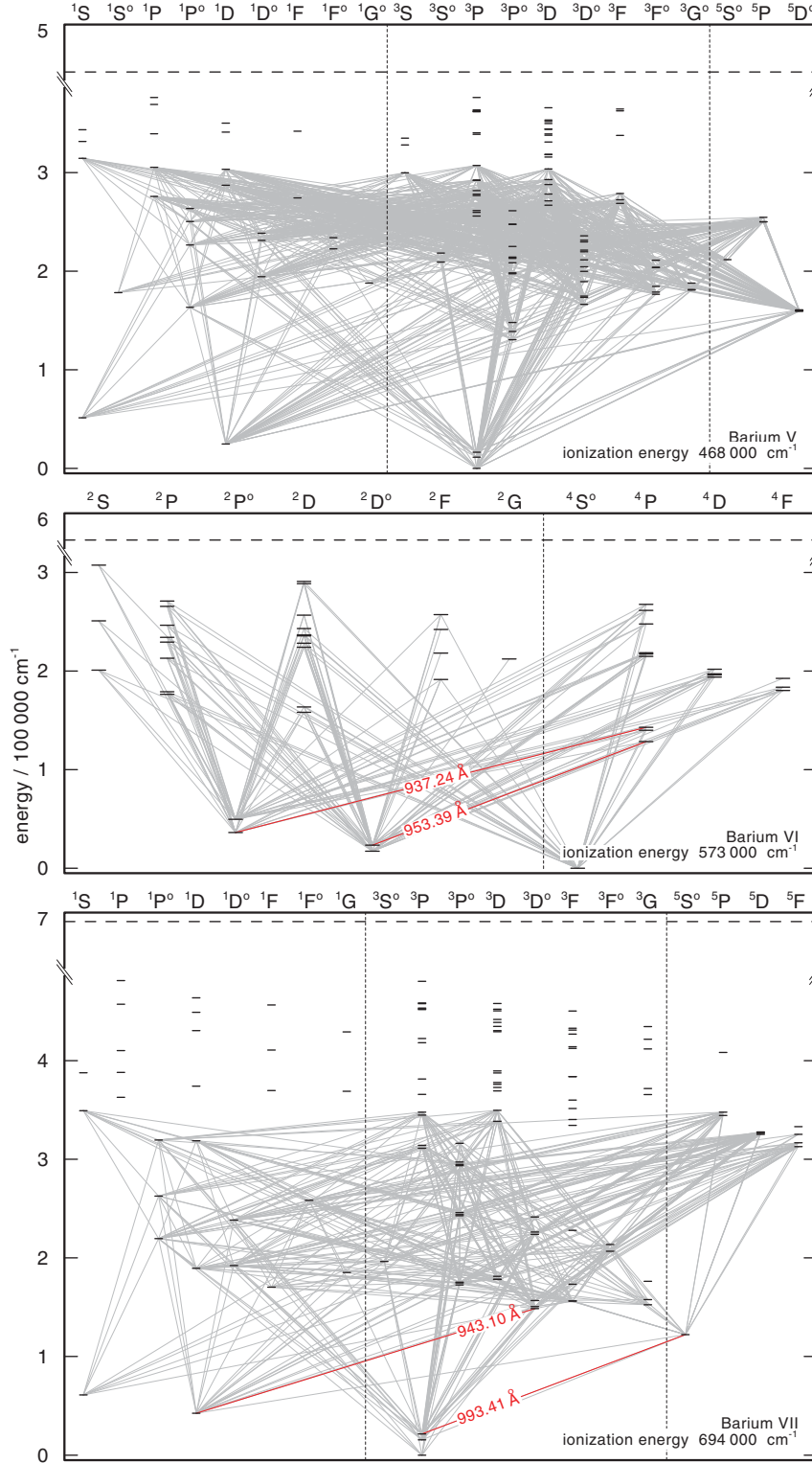
[8] http://dc.g-vo.org/theossa

Fig. 1. Grotrian diagrams of our Ba V (*top*), Ba VI (*middle*), and Ba VII (*bottom*) model ions. Horizontal bars indicate levels, gray lines represent radiative transitions with known f values (Tables 1–3). Our strategic Ba VI and Ba VII lines in the FUSE wavelength range (Fig. 6) are labeled with their wavelengths. The long-dashed, horizontal lines in each panel show the ionization energies of $468\,000\,\mathrm{cm}^{-1}$, $573\,000\,\mathrm{cm}^{-1}$, and $694\,000\,\mathrm{cm}^{-1}$ of Ba V, Ba VI, and Ba VII, respectively.

The start models for our calculations are the most elaborated model atmospheres for both stars (Rauch et al. 2014). As our main model-atmosphere program would not compile if the array sizes were increased to accommodate the high number of atomic levels treated in NLTE and the high number of radiative and collisional transitions, (cf. Rauch et al. 2014), we simply reduced the number of the Zn levels treated in NLTE to one per ion to create a TMAP executable. Because the Zn opacities were already considered in detail in our start models, the atmospheric structure and the background opacities are well modeled. To calculate the NLTE occupation numbers of Ba, we performed line-formation calculations, i.e., we kept temperature and density
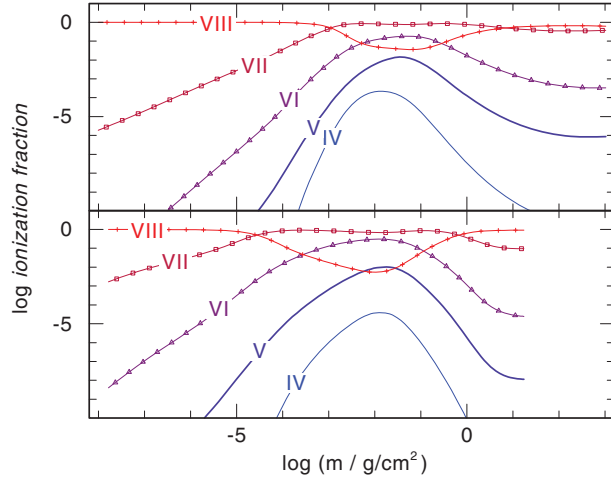
Fig. 2. Ba ionization fractions in our models for G191−B2B (*top panel*, H+Ba) and RE 0503−289 (*bottom panel*, He+Ba). m is the column mass, measured from the outer boundary of our model atmospheres.

structure of our model-atmospheres fixed. Since the impact of Ba on the atmospheric structure of our H+Ba and He+Ba test models (Sect. 5) was found to be marginal, this is the best practice. For the subsequent SED calculations, we considered the complete model ions and resumed the missing Zn occupation numbers from the start models.

5. Preliminary analysis

For a preliminary analysis, we calculated models that consider only H+Ba and He+Ba for G191−B2B ($T_{eff} = 60\,000$ K, $\log g = 7.6$) and RE 0503−289 ($T_{eff} = 70\,000$ K, $\log g = 7.5$), respectively. The Ba abundance was 1.5×10^{-5} (mass fraction, about 1000 times solar, Asplund et al. 2009) in both models. Figure 2 shows the respective Ba ionization fractions. Ba VII is the dominating ionization stage in the line forming region ($-2.5 \lesssim \log m \lesssim 0.5$). In the case of G191−B2B, the H+Ba spectrum shows two prominent lines in the FUV, Ba VII $\lambda\lambda$ 943.10, 993.41 Å, and several much weaker Ba VI and Ba VII lines (Fig. 3). For RE 0503−289, Ba VII λ 993.41 Å is the strongest line in the He+Ba, but some weaker Ba VI and Ba VII lines are also visible.

For the wavelengths higher than the FUSE wavelength range, an adequate observation is only available for G191−B2B (Sect. 3). Our test model shows a rich Ba VII spectrum within 1150 Å $\leq \lambda \leq 1780$ Å for this star, and a few weak Ba V-VI lines in addition (Fig. 4). The model spectrum for RE 0503−289 shows the same lines, with deviations in the relative line strengths. We note that all these lines are much weaker than the four Ba VI-VII lines in the FUSE wavelength range (Fig. 3).

The preliminary models cannot be used for a reliable abundance determination because the neglected metals result in an unrealistic atmospheric structure (Fig. 5), and their missing background opacities have a strong impact on the strengths of the Ba lines. Therefore, we performed a precise determination of the Ba abundances based on detailed atomic data and elaborated model atmospheres (Sect. 6).
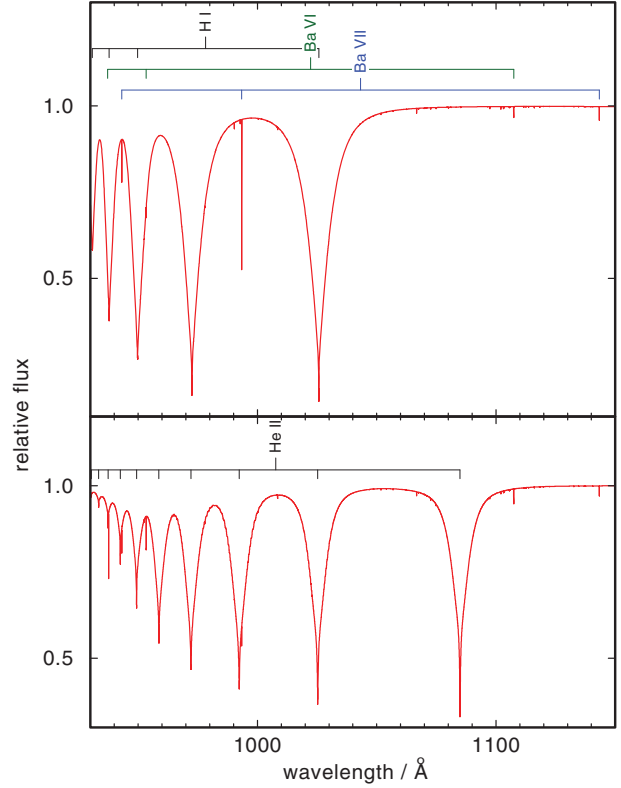

Fig. 3. Synthetic spectra (normalized to the models's continuum fluxes) of our H+Ba model for G191−B2B (*top panel*) and our He+Ba model for RE 0503−289 (*bottom panel*). All synthetic spectra displayed in this paper are convolved with Gaussians to simulate the instruments' resolution. Here, for FUSE, we used an FWHM (full width at half maximum) of 0.06 Å.
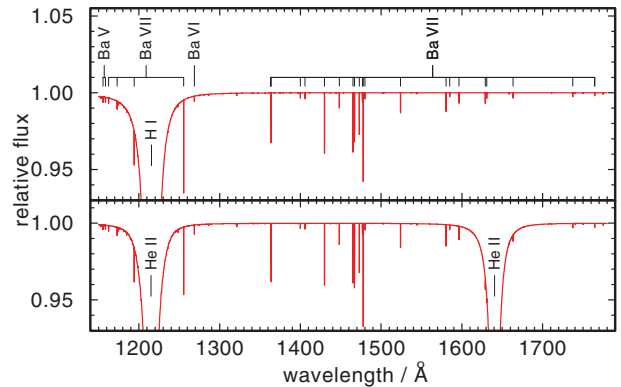

Fig. 4. Same as Fig. 3 (*top*: G191−B2B, *bottom*: RE 0503−289), to simulate the HST/STIS spectrum (*FWHM* = 0.01 Å).

6. The photospheric Ba abundances in G191−B2B and RE 0503−289

We determine the Ba abundances of G191−B2B and RE 0503−289 from their FUSE observations. Figure 6 shows that we can well reproduce the Ba lines with Ba mass fractions of $4.0 \pm 0.5 \times 10^{-6}$ and $3.5 \pm 0.5 \times 10^{-4}$, respectively. These values are strongly over-solar (23 000 times and 265 times, respectively, Asplund et al. 2009) but in line with the determined
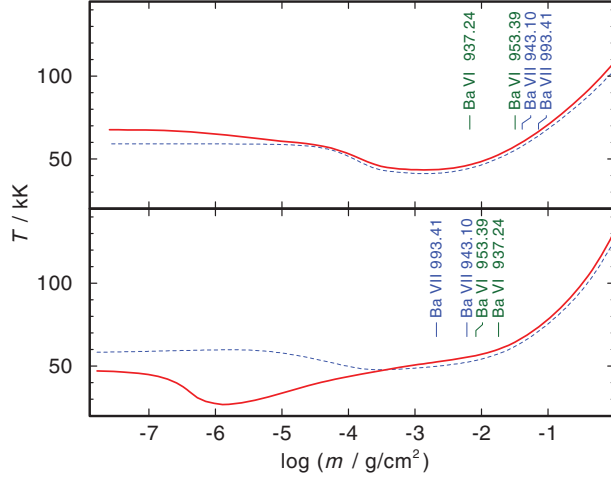
Fig. 5. Temperature structures of the final model atmospheres of G191−B2B (*top panel*, thick, red line; Rauch et al. 2013, H, He, C, N, O, Al, Si, P, S, Ca, Sc, Ti, V, Cr, Mn, Fe, Co, Ni, Zn, and Ge opacities considered) and RE 0503−289 (*bottom panel*, thick, red line; Rauch et al. 2014, He, C, N, O, Ca, Sc, Ti, V, Cr, Mn, Fe, Co, Ni, Zn, Ge, Kr, and Xe). The dashed, blue lines show the temperature structures of H+Ba (*top*) and He+Ba (*bottom*) models calculated with the same T_{eff} and $\log g$ like the final models, respectively. The formation depths (i.e., $\tau = 1$) of the cores of our strategic of the cores of our strategic Ba VI − VII lines in FUSE's wavelength range are marked.

abundances of other trans-iron elements (e.g., Werner et al. 2012; Rauch et al. 2013, Fig. 7). It is worthwhile to note, that the Ba VI/Ba VII ionization equilibrium is very well reproduced for RE 0503−289.

In addition to the metals' background opacity in the final model mentioned above, the determined Ba abundance of G191−B2B is only a fourth of that used in our test model (Fig. 4) and, thus, the lines in the wavelength interval 1145 Å < λ < 1750 Å are weaker in the models, respectively. Figure 8 shows a section of the spectrum where our test models predicted the strongest lines (Fig. 4). A comparison to a model, that was calculated without Ba, shows that in this section only Ba VII λ 1472.96 Å is a weak, isolated line that is visible in our model. Its strength is comparable to the low noise of the observed spectrum and, thus, we can determine an upper limit for the Ba abundance which is the same upper value determined from the FUSE spectrum (see above). For RE 0503−289, the determined Ba abundance is more than 20 times higher than in our test model (Fig. 4) and, thus, the potential identification of Ba lines in this wavelength range is most likely. A high-resolution, high-signal-to-noise HST/STIS UV spectrum of RE 0503−289 is highly desirable.

7. Results and conclusions

We determined precisely the photospheric Ba abundances in the DA-type white dwarf G191−B2B ($4.0 \pm 0.5 \times 10^{-6}$) and in the DO-type white dwarf RE 0503−289 ($3.5 \pm 0.5 \times 10^{-4}$). These strongly supersolar abundance values are in line with those of other trans-iron elements in both stars (Fig. 7).

Ba is one of the most massive s-process (slow neutron capture) elements synthesized by low-mass ($\approx$1–3 $M_\odot$) AGB stars (e.g., Lattanzio & Lugaro 2005). The s-process leads to abundance peaks at approximate mass numbers of 88, 138, and 208
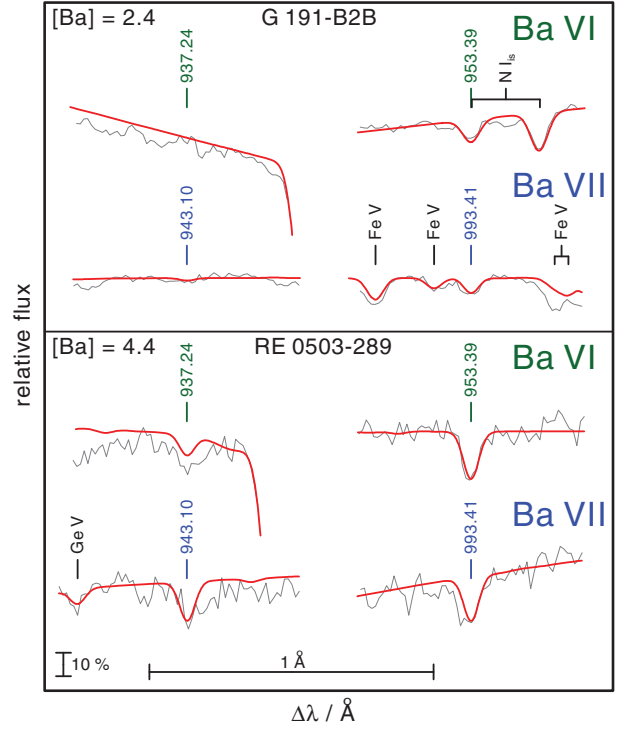

Fig. 6. Comparison of the theoretical line profiles of the strongest Ba VI and Ba VII lines with the FUSE observation. The synthetic spectra were normalized to the observed local continuum fluxes. *Top*: G191−B2B, *bottom*: RE 0503−289. [X] denotes log (mass fraction/solar mass fraction) of species X.
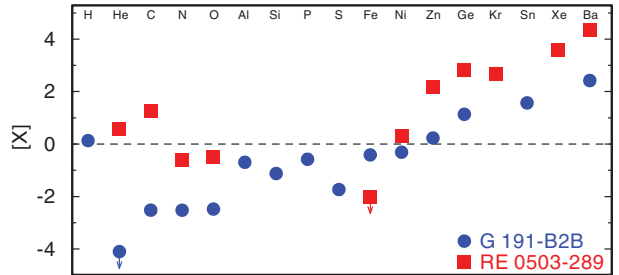

Fig. 7. Photospheric abundances of G191−B2B (bullets, Rauch et al. 2013, 2014) and RE 0503−289 (squares, Werner et al. 2012; Rauch et al. 2012, 2014) compared with solar values (Asplund et al. 2009). The abundance uncertainties are about 0.2 dex in general. The arrows denote upper limits. The dashed line indicates the solar values.

(West & Heger 2013; Karakas et al. 2014) due to closed neutron shells. Sr, Ba (isotopes from ^{128}Ba to ^{140}Ba), and Pb are located at these peaks and are used to represent the scaling of the s-process elements. Therefore, the Ba abundance determined in the hot WDs G191−B2B and RE 0503−289 establishes a new constraint for AGB and post-AGB stellar evolution and will help to understand the extremely strong metal enrichment.

The identification of Ba lines in this paper was only possible because reliable transition probabilities for Ba V, Ba VI, and Ba VII were calculated. Analogous calculations for other highly ionized trans-iron elements is a pre-requisite for further identifications an abundance analyses. The precise measurement of their spectra, i.e., their lines' wavelengths and relative strengths,
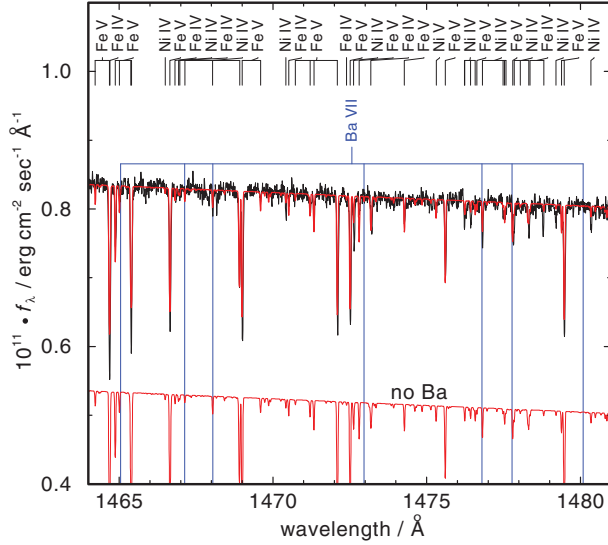
Fig. 8. Section of the HST/STIS spectrum of G191−B2B compared with our synthetic spectrum. The thin (blue) model at the bottom is calculated without Ba. The identified Fe and Ni lines and the Ba VII lines are marked at *top*.

as well as the determination of level energies and the calculation of transition probabilities remains a challenge for atomic and theoretical physicists.

References

Asplund, M., Grevesse, N., Sauval, A. J., & Scott, P. 2009, ARA&A, 47, 481
Cowan, R. D. 1981, The theory of atomic structure and spectra (Berkeley, CA, University of California Press)
Fraga, S., Karwowski, J., & Saxena, K. M. S. 1976, Handbook of Atomic Data (Amsterdam: Elsevier)
Karakas, A. I., Marino, A. F., & Nataf, D. M. 2014, ApJ, 784, 32
Lattanzio, J. C., & Lugaro, M. A. 2005, Nucl. Phys. A, 758, 477
Quinet, P., Palmeri, P., Biémont, E., et al. 1999, MNRAS, 307, 934
Quinet, P., Palmeri, P., Biémont, E., et al. 2002, in Proc. Rare Earths' 2001 Conference, J. Alloys Comp., 344, , eds. M. A. Leskela, M. F. Reid, H. B. Silber, & L. B. Zinner, 255
Rauch, T., & Deetjen, J. L. 2003, in Stellar Atmosphere Modeling, eds. I. Hubeny, D. Mihalas, & K. Werner, ASP Conf. Ser., 288, 103
Rauch, T., Werner, K., Biémont, É., Quinet, P., & Kruk, J. W. 2012, A&A, 546, A55
Rauch, T., Werner, K., Bohlin, R., & Kruk, J. W. 2013, A&A, 560, A106
Rauch, T., Werner, K., Quinet, P., & Kruk, J. W. 2014, A&A, 564, A41
Sharma, M. K., Rahimullah, K., & Tauheed, A. 2014, J. Quant. Spectr. Rad. Transf., 133, 281
Sharma, M. K., Tauheed, A., & Rahimullah, K. 2013, J. Quant. Spectr. Rad. Transf., 119, 32
Tauheed, A., & Joshi, Y. N. 1994, Phys. Scr, 49, 335
Werner, K., Deetjen, J. L., Dreizler, S., et al. 2003, in Stellar Atmosphere Modeling, eds. I. Hubeny, D. Mihalas, & K. Werner, ASP Conf. Ser., 288, 31
Werner, K., Rauch, T., Ringat, E., & Kruk, J. W. 2012, ApJ, 753, L7
West, C., & Heger, A. 2013, ApJ, 774, 75